

# SATELLITE & MESOMETEOROLOGY RESEARCH PROJECT

Department of the Geophysical Sciences  
The University of Chicago

ANGULAR DEPENDENCE OF ALBEDO FROM STRATIFORM CLOUDS  
AS MEASURED BY TIROS IV SCANNING RADIOMETERS

by

Åsmund Rabbe

**N66 32553**

(ACCESSION NUMBER)

(THRU)

**27**

(PAGES)

(CODE)

**20**

(CATEGORY)

**CR-76799**

(NASA CR OR TMX OR AD NUMBER)

FACILITY FORM 602

GPO PRICE \$ \_\_\_\_\_

CFSTI PRICE(S) \$ \_\_\_\_\_

Hard copy (HC) 2.00

Microfiche (MF) .50

# 853 July 65

**SMRP Research Paper**

NUMBER 58

June 1966

# MESOMETEOROLOGY PROJECT --- RESEARCH PAPERS

1. • Report on the Chicago Tornado of March 4, 1961 - Rodger A. Brown and Tetsuya Fujita
2. • Index to the NSSP Surface Network - Tetsuya Fujita
3. • Outline of a Technique for Precise Rectification of Satellite Cloud Photographs - Tetsuya Fujita
4. • Horizontal Structure of Mountain Winds - Henry A. Brown
5. • An Investigation of Developmental Processes of the Wake Depression Through Excess Pressure Analysis of Nocturnal Showers - Joseph L. Goldman
6. • Precipitation in the 1960 Flagstaff Mesometeorological Network - Kenneth A. Styber
7. \*\* On a Method of Single- and Dual-Image Photogrammetry of Panoramic Aerial Photographs - Tetsuya Fujita
8. A Review of Researches on Analytical Mesometeorology - Tetsuya Fujita
9. Meteorological Interpretations of Convective Neph systems Appearing in TIROS Cloud Photographs - Tetsuya Fujita, Toshimitsu Ushijima, William A. Hass, and George T. Dellert, Jr.
10. Study of the Development of Prefrontal Squall-Systems Using NSSP Network Data - Joseph L. Goldman
11. Analysis of Selected Aircraft Data from NSSP Operation, 1962 - Tetsuya Fujita
12. Study of a Long Condensation Trail Photographed by TIROS I - Toshimitsu Ushijima
13. A Technique for Precise Analysis of Satellite Data; Volume I - Photogrammetry (Published as MSL Report No. 14) - Tetsuya Fujita
14. Investigation of a Summer Jet Stream Using TIROS and Aerological Data - Kozo Ninomiya
15. Outline of a Theory and Examples for Precise Analysis of Satellite Radiation Data - Tetsuya Fujita
16. Preliminary Result of Analysis of the Cumulonimbus Cloud of April 21, 1961 - Tetsuya Fujita and James Arnold
17. A Technique for Precise Analysis of Satellite Photographs - Tetsuya Fujita
18. Evaluation of Limb Darkening from TIROS III Radiation Data - S.H.H. Larsen, Tetsuya Fujita, and W.L. Fletcher
19. Synoptic Interpretation of TIROS III Measurements of Infrared Radiation - Finn Pedersen and Tetsuya Fujita
20. TIROS III Measurements of Terrestrial Radiation and Reflected and Scattered Solar Radiation - S.H.H. Larsen, Tetsuya Fujita, and W.L. Fletcher
21. On the Low-level Structure of a Squall Line - Henry A. Brown
22. Thunderstorms and the Low-level Jet - William D. Bonner
23. The Mesoanalysis of an Organized Convective System - Henry A. Brown
24. Preliminary Radar and Photogrammetric Study of the Illinois Tornadoes of April 17 and 22, 1963 - Joseph L. Goldman and Tetsuya Fujita
25. Use of TIROS Pictures for Studies of the Internal Structure of Tropical Storms - Tetsuya Fujita with Rectified Pictures from TIROS I Orbit 125, R/O 128 - Toshimitsu Ushijima
26. An Experiment in the Determination of Geostrophic and Isallobaric Winds from NSSP Pressure Data - William Bonner
27. Proposed Mechanism of Hook Echo Formation - Tetsuya Fujita with a Preliminary Mesosynoptic Analysis of Tornado Cyclone Case of May 26, 1963 - Tetsuya Fujita and Robbi Stuhmer
28. The Decaying Stage of Hurricane Anna of July 1961 as Portrayed by TIROS Cloud Photographs and Infrared Radiation from the Top of the Storm - Tetsuya Fujita and James Arnold
29. A Technique for Precise Analysis of Satellite Data, Volume II - Radiation Analysis, Section 6. Fixed-Position Scanning - Tetsuya Fujita
30. Evaluation of Errors in the Graphical Rectification of Satellite Photographs - Tetsuya Fujita
31. Tables of Scan Nadir and Horizontal Angles - William D. Bonner
32. A Simplified Grid Technique for Determining Scan Lines Generated by the TIROS Scanning Radiometer - James E. Arnold
33. A Study of Cumulus Clouds over the Flagstaff Research Network with the Use of U-2 Photographs - Dorothy L. Bradbury and Tetsuya Fujita
34. The Scanning Printer and Its Application to Detailed Analysis of Satellite Radiation Data - Tetsuya Fujita
35. Synoptic Study of Cold Air Outbreak over the Mediterranean using Satellite Photographs and Radiation Data - Aasmund Rabbe and Tetsuya Fujita
36. Accurate Calibration of Doppler Winds for their use in the Computation of Mesoscale Wind Fields - Tetsuya Fujita
37. Proposed Operation of Instrumented Aircraft for Research on Moisture Fronts and Wake Depressions - Tetsuya Fujita and Dorothy L. Bradbury
38. Statistical and Kinematical Properties of the Low-level Jet Stream - William D. Bonner
39. The Illinois Tornadoes of 17 and 22 April 1963 - Joseph L. Goldman
40. Resolution of the Nimbus High Resolution Infrared Radiometer - Tetsuya Fujita and William R. Bandeen
41. On the Determination of the Exchange Coefficients in Convective Clouds - Rodger A. Brown

• Out of Print

\*\* To be published

(Continued on back cover)

SATELLITE AND MESOMETEOROLOGY RESEARCH PROJECT

Department of the Geophysical Sciences

The University of Chicago

ANGULAR DEPENDENCE OF ALBEDO FROM STRATIFORM CLOUDS  
AS MEASURED BY TIROS IV SCANNING RADIOMETERS

by

Åsmund Rabbe

SMRP Research Paper #58

June

1966

The research reported in this paper has been supported by the  
National Aeronautics and Space Administration under grant NASA NsG 333.

ANGULAR DEPENDENCE OF ALBEDO FROM STRATIFORM CLOUDS  
AS MEASURED BY TIROS IV SCANNING RADIOMETERS<sup>1</sup>

Åsmund Rabbe

Department of the Geophysical Sciences

The University of Chicago

Chicago, Illinois

ABSTRACT

32553

Pictures and radiation data from two orbits of TIROS IV have been used in this study to show the anisotropy in the albedo of low stratiform clouds. In order to scan the same clouds from two different directions we have used the radiation data when the satellite was in an alternating mode while the floor and wall sensors scanned the earth successively. To express the anisotropy we have used the specular angle,  $\omega$ , and the backscattering angle,  $\psi_0$ , as parameters. The results show that the albedo is dependent on these two parameters, particularly the specular angle.

1. Introduction.

The scattering and reflection of light in the atmosphere have been the subject of several studies. During World War II, Waldram (1945) made some experiments with a nephelometer and calculated the polar scatter index. He found a pronounced maximum at  $0^\circ$ , or in the forward scattering direction; a secondary maximum at  $180^\circ$ , or in the backward scattering direction; and a minimum around  $90^\circ$ , depending on the purity of the air. Deirmendjian (1962) obtained results very close to Waldram's; however, his minimum was located at a scattering angle near  $110^\circ$ . He also found a pronounced, relatively narrow maximum around  $143^\circ$ , which he explained as resulting from the fogbow, or white rainbow.

With the advent of the TIROS satellites with radiometers aboard, much radiation data have become available for such studies. Several authors have shown that radiation

---

<sup>1</sup>The research reported in this paper has been supported by the National Aeronautics and Space Administration under grant NASA NsG 333.

data obtained from Channel 2 ( $8-12\mu$ ), combined with those from Channel 3 ( $0.25-6.0\mu$ ), are useful in interpreting cloud systems and weather patterns on synoptic charts. The energy received by Channel 3 depends mainly on the reflecting surface, but this is not the only dependency. The energy is also a function of the solar zenith angle, the satellite zenith angle, and the relative azimuth.

Bartman et. al. (1964) measured the reflected and scattered radiation received by a TIROS IV radiometer from a high altitude (34 km) balloon flight in June, 1962. The radiation came from a rather uniform stratocumulus cover. Their readings covered scattering angles from  $40^\circ$  to  $160^\circ$ . Two maximum values, located at scattering angles of  $40^\circ$  and above  $140^\circ$ , respectively, were obtained. The minimum was located between  $110^\circ$  and  $120^\circ$ .

Larsen et. al. (1963) computed backscattering angles (the angle between incident and outgoing beam) for initial and complementary scans from one orbit of TIROS III. They kept the satellite zenith angles constant and assumed the solar zenith to be constant because of the small time interval. The backscattering angles for initial scans varied from  $15^\circ$  to  $40^\circ$ ; for the complementary scans, there was only a slight variation around  $70^\circ$ . The energy values received from the same scan spot during the initial scans were higher than those received during the complementary scans. This is in agreement with the results of Deirmendjian and Bartman.

Viezee and Davis (1965) used one orbit of TIROS IV to show anisotropy in the backscattered light when the satellite is in an alternating mode (i.e., floor and wall sensor are scanning the earth successively). The scattering angles for floor and wall sensors varied from  $131^\circ$  to  $78^\circ$  and from  $100^\circ$  to  $53^\circ$  respectively. They found that the energy coming to the wall sensor was much higher than that coming to the floor sensor.

In this study we too have used two orbits of TIROS IV when the satellite was in an alternating mode, so that we could apply the data from both floor and wall sensors. On the basis of satellite pictures, synoptic observations, and satellite radiation data, we have been able to distinguish between different kinds of cloud surfaces. The purpose has been to see if there exist any significant differences in the reflecting properties of low stratiform cloud surfaces when they are viewed by the satellite from different directions. Although this problem has been the subject of much research, no completely satisfactory solution has as yet been offered.

## 2. Variation in Albedo of Stratoform Clouds as a Function of the Specular Angles.

The scattering and the backscattering angles, which are complementary, have been used by most authors to express the angular dependence of the outgoing shortwave radiation from the earth. The backscattering angle,  $\psi_b$ , can be expressed by

$$\cos \psi_b = \cos \zeta_* \cos \zeta_\bullet + \sin \zeta_* \sin \zeta_\bullet \cos \Delta\alpha \quad (1)$$

where  $\zeta_*$  and  $\zeta_\bullet$  are the zenith angles of the sun and the satellite, respectively, and  $\Delta\alpha$  is the relative azimuth (Fujita, 1963). The scattering and backscattering angles are useful parameters for expressing this angular dependence if the short-wave radiation picked up by the satellite is mainly scattered light. This may occur with very large solar zenith angles and with incoming light scattered by diffuse cirrus cloud surfaces. But in the case of a low stratiform cloud surface, which consists primarily of water droplets, reflection becomes by far the most important part of the short-wave radiation received by the satellite. Because of this we have found it useful to introduce another angle,  $\omega$ , the specular angle. This is the angle between the radiometer axis and the specular reflection axis (Fig. 1). The specular angle is found from

$$\cos \omega = \cos \zeta_* \cos \zeta_\bullet + \sin \zeta_* \sin \zeta_\bullet \cos (180^\circ - \Delta\alpha) \quad (2)$$

Since the maximum albedo, at least from a stratiform cloud surface, is assumed to coincide with the specular reflection axis, it becomes obvious that this angle has a significant physical meaning. If this maximum decreased uniformly out from the specular reflection axis in all directions, the specular angle would be the only independent variable. This is not plausible; it is more likely that the albedo is determined by a more complicated function of solar zenith angle, satellite zenith angle, and the relative azimuth. We will therefore only assume that the specular angle  $\omega$  is a relatively good first approximation for the expression of this angular dependence, at least for small values of  $\omega$ .

In the case of an alternating mode (Fig. 1), where the two sensors look at the earth from quite different directions, it is convenient to express the angular dependence with the specular angle for one of the sensors and with the backscattering angle for the other. The reason for this is the existence of a small backward scattered maximum in the direction towards the sun, and another advantage is that the variation in both angles is kept within relatively low values.

### 3. Results of Dual Measurements by Floor and Wall Sensors During Two TIROS IV Orbits.

When the TIROS satellite's spin axis is oriented approximately parallel to the earth's surface, the floor and the wall sensors scan the earth alternately. The wall sensor may scan an area first; then about three or four minutes later the floor sensor will scan approximately the same area. The overlapping area increases with a decreasing angle between the primary lines and the TSP track.

The orbits used in this study are nos. 143 and 200 of TIROS IV on 18 and 22 February 1962, respectively; and the geographical area covered is a portion of the Atlantic Ocean and West Africa, limited by  $30^{\circ}\text{W}$  to  $5^{\circ}\text{W}$  and  $50^{\circ}\text{N}$  to  $15^{\circ}\text{N}$ . The data are presented on sigma-t printout sheets produced by the Fujita scanning printer (Fujita, 1964). Longitude and latitude lines, as well as coastlines and other landmarks, are transferred to the printout sheets. Because of the conical scan geometry used in TIROS, the distortion of the grid lines will be in opposite directions for the floor and the wall sensors. This may cause confusion to the reader, who may prefer to see the data transferred to a standard map projection. On the other hand, this manner of presentation shows more clearly the many difficulties and uncertainties involved in the interpretation of the data, which may be effected by limb darkening space contamination, scan-spot size, etc.

Both of the analyzed orbits had useable photographs of the area of interest. These have been utilized in constructing the cloud composite charts in Figs. 2 and 11. The pictures have been transferred to the same kind of distorted map that was used for the floor sensor radiation data, because the floor sensor's principal lines and the optical principal lines nearly coincide. The high tilt made it rather difficult to construct a complete cloud chart from the pictures alone; in the uncertain areas, however, the available synoptic data combined with the radiation data have been used to complete the cloud charts. These areas have been singled out by hatching.

The pictures alone do not enable us to distinguish clearly between the different cloud types, but when combined with the synoptic data they give a fairly good idea about the clouds in question. The analyzed Channel 2 radiation data give additional information about the cloud heights, and can be used to confirm what has been learned from the two other sources. Using this method it was found that the clouds in the

areas indicated by A, B, C, in orbit 200 (Fig. 2) consisted of low stratiform clouds, while those in the areas indicated by D and E were altostratus or altocumulus, and cirrostratus, respectively. In orbit 143 (Fig. 11) the clouds in the areas indicated by F, G, and H all consisted of low stratiform clouds.

Figures 3 and 4 show the albedo,  $A$ , in percentage, obtained in orbit 200 from the wall and the floor sensors, respectively. The values have not been corrected for sensor degradation, because the correction that could be obtained would be rather uncertain, and also because we were mainly interested in the relative values between the wall and floor sensor. However, the readings have been corrected for 20% space contamination, and the values farther out towards the apparent horizon and beyond have been discarded. Isolines for specular angles and backscattering angles have been drawn on the wall and the floor sensor charts, respectively. The cloudy areas indicated by capital letters are outlined in both maps; these areas are seen to coincide with those of maximum albedo.

Figures 5 and 6 show the effective radiant emittances,  $\bar{W}$ , obtained in the same orbit from the wall and the floor sensor respectively. These values have been corrected for sensor degradation, but not for water vapor, ozone, limb darkening, etc. The readings in the cloudy areas A, B, and C indicate rather small differences from the virtually clear areas in the sea, while the readings in the areas D and E are significantly lower. The cirrus area E gives a minimum energy value of 18 watts  $m^{-2}$  in both sensors, which corresponds to a temperature of approximately  $-25^{\circ}C$ . The soundings from the area indicate a cirrus temperature of  $-45^{\circ}C$ , which means that the energy coming to the satellite is strongly influenced by the background radiation.

Figures 12 and 13 show the albedo values obtained in orbit 143 from the wall and from the floor sensors, respectively. The explanations of Figs. 3 and 4, orbit 200, are more or less valid for these figures also.

#### 4. Use of Effective Psuedo-radiant Emittance in Determining Cloud Albedo Excluding Background Albedo.

As the composite cloud charts in Figs. 2 and 11 indicate, the cloud covers investigated are not all solid, but instead are broken or scattered. The albedo  $A$  measured by Channel 3 from many of the areas therefore must have originated partly from the clouds and partly from the background. In order to eliminate the effect



of the background albedo we will make use of Eq. (3) which was derived from Eqs. (11) and (13) of Fujita and Grandoso (1966). Thus,

$$A_c = \frac{1}{\beta \bar{\pi}} (\bar{\pi} \beta A_b + \bar{B}_b - \bar{B}_c) \quad (3)$$

where  $A_c$  is the cloud albedo,  $\beta$  is a coefficient varying between 0 and 1.0 depending upon the type and thickness of the cloud, and is equivalent to  $\rho$  in Fujita and Grandoso;  $A_b$  is the background albedo,  $B_b$  is the effective background radiant emittance, and  $B_c$  is the effective cloud radiant emittance.

$$\bar{\pi} = \frac{\bar{B}_b - \bar{W}}{A - A_b}$$

is defined as the effective pseudo-radiant emittance; this is found to be a useful quantity in determining the type of clouds. It can immediately be seen that the value of  $\bar{\pi}$  increases with increasing cloud heights, and it also increases with decreasing cloud thickness and increasing cloud diffuseness. From Eq. (3) the cloud albedo can be found, if  $\beta$ ,  $A_b$ ,  $B_b$ , and  $B_c$  are known. In this particular case we are mainly interested in the albedo from low stratiform clouds over a water surface. In the case of low, relatively thick stratus clouds  $\beta$  is expected to be approximately equal to 1 and the background albedo from water  $A_b$  is assumed to equal 0.01 at least when the solar zenith angle is less than  $60^\circ$ . If we take the ratio between the cloud albedo for the wall sensor and that for the floor sensor under these conditions, we obtain

$$\frac{A^{WL}}{A^{FL}} = \frac{\bar{\pi}^{FL}}{\bar{\pi}^{WL}} \quad (4)$$

This means that we only have to compute  $\bar{\pi}$  for both floor and wall sensors in order to obtain the ratio between the cloud albedo coming to the two sensors. In order to compute  $\bar{\pi}$  we must know the background albedo  $A_b$  and the effective background radiant emittance  $B_b$ . In Figs. 7 and 8 the background albedo  $A_b$  for both sensors in orbit 200 has been estimated. The water albedo has been assumed to be 0.01, which is plausible, as long as the solar zenith angle stays below  $60^\circ$ . The Sahara Desert, which is indicated by stippling on the chart, gives a very high background albedo  $A_b$ , which more or less coincides with the actual albedo  $A$  because the area is apparently cloudless. In Figs. 9 and 10 the effective background radiant emittances have been estimated for both wall and floor sensor in orbit 200. The effective radiant emittance from water is close to  $35 \text{ watts m}^{-2}$  for the main part of the area, except

near the horizon where the limb darkening effect occurs. It may also be noted that the Sahara Desert is relatively cold compared to its surroundings; this is due to the early time of day and the high reflectance from the sand. From the maps in Figs. 3, 5, 7, and 9, and from the maps in Figs. 4, 6, 8, and 10, we are able to compute  $\bar{\pi}$  for wall sensor and floor sensor in orbit 200, respectively.

## 5. Discussion of Anisotropic Albedo Obtained.

The results of the  $\bar{\pi}$  computations are shown in Figs. 14 and 15 for orbit 200 and in Figs. 16 and 17 for orbit 143. The values of  $\bar{\pi}$  in the stratus cloud areas A, B, and C in Figs. 14 and 15 are relatively low and uniform for both sensors; moreover, the values of  $\bar{\pi}^{\text{WL}}$  seem to be mainly a little lower than those of  $\bar{\pi}^{\text{FL}}$ . The values of  $\bar{\pi}$  in the cirrus area are high in both sensors, but relatively the  $\bar{\pi}^{\text{FL}}$  values are almost twice as large as those of  $\bar{\pi}^{\text{WL}}$ . The stratocumulus cloud cover at D shows values of  $\bar{\pi}$  about three times as high in the floor sensor as in the wall sensor. This latter may be caused by several things; the satellite zenith angle for the wall sensor is above  $70^\circ$  in this area, which makes the computation of  $\bar{\pi}$  uncertain because of limb darkening, scanspot size, etc.; furthermore the relative azimuth is close to  $180^\circ$  in the area and the specular angle is small, around  $20^\circ$ . In Figs. 16 and 17 the  $\bar{\pi}$  values for wall and floor sensors in orbit 143 are presented. These values are consistently a little lower than those from the stratus area in orbit 200; this is mainly due to higher albedo but partly due to lower cloud heights.

To find the angular dependence of the albedo we have used Eq. (4) for the areas covered with low stratiform clouds over water. The areas of cirrus and alto-cumulus have been excluded, primarily because we do not know the value of  $\beta$  for these clouds. The results of these computations are shown in Figs. 18 and 19. The ratio  $A_c^{\text{WL}}/A_c^{\text{FL}}$  (between the cloud albedo obtained by the wall sensor and the cloud albedo obtained by the floor sensor) has been plotted as a function of the specular angle  $\omega^{\text{WL}}$  for the wall sensor, and the backscattering angle  $\psi_b^{\text{FL}}$  for the floor sensor. The number in each square is an average over a  $10^\circ$  interval, for both angles; the number in parentheses indicates how many values were averaged.

In orbit 200 the backscattering angles  $\psi_b^{\text{FL}}$  remain almost constant between  $10^\circ$  and  $20^\circ$ , while the specular angles  $\omega^{\text{WL}}$  vary from  $40^\circ$  down to almost  $0^\circ$ . The ratio  $A_c^{\text{WL}}/A_c^{\text{FL}}$  should then be primarily a function of the specular angle. As can be seen, the ratio increases gradually for lower values of  $\omega^{\text{WL}}$ ; it reaches a maximum of

1.55 when the specular angle is between  $0^\circ$  and  $10^\circ$ . In orbit 143 both the backscattering angle and the specular angle vary between  $10^\circ$  and  $70^\circ$ . As in orbit 200, the ratio  $A_c^{WL}/A_c^{FL}$  increases as the specular angle decreases, and it also increases as the backscattering angle decreases. In the regions of  $10^\circ$  to  $20^\circ$  backscattering angle, and of  $40^\circ$  to  $70^\circ$  specular angle, the ratio is close to 1 which should indicate isotropic conditions.

## 6. Conclusions.

Evidence of anisotropy in the albedo from low stratiform clouds seems obvious from the results obtained in the two orbits. Since these clouds consist mainly of water droplets, reflection is by far the most important part of the short-wave radiation measured by the satellite. The specular angle  $\omega$ , which is a measure of the deviation from the specular reflection axis, seems to be an important and convenient parameter to express this dependence, even though we believe the exact relationship to be a more complicated function of the solar zenith angle, satellite zenith angle, and relative azimuth. The results obtained do not allow many generalizations, because of the small sample of data, but it seems evident that the anisotropy becomes more and more significant as the specular angle  $\omega$  decreases. The orbit 143 data seem to suggest nearly isotropic conditions when the specular angle  $\omega^{WL}$  exceeds  $40^\circ$ - $50^\circ$ , but this certainly has to be substantiated by further research. The backward scattering or reflecting maximum towards the sun seems also to be a reality, since the ratio  $A_c^{WL}/A_c^{FL}$  increases with decreasing backscattering angles  $\psi_b^{FL}$ .

The data from cirrus and altocumulus areas in orbit 200 also suggest a strong anisotropy in the albedo. Investigation of these clouds is, however, more complex, as their coefficient  $\beta$  is less than 1, and as their tops consist mainly of ice crystals which may scatter the light more than they reflect it.

## ACKNOWLEDGEMENTS

The author wishes to thank Dr. Fujita for his valuable advice and suggestions offered during the course of this research.

## REFERENCES

- Bartman, F. L., L. W. Chaney, P. A. Titus, and M. G. Whybra, 1964: Infrared and visible radiation measurements by radiometer and interferometer on high altitude balloon flights at 34-km altitude. High Altitude Engineering Laboratory, Univ. of Michigan, 16 pp.
- Deirmendjian, D., 1962: Scattering and polarization properties of polydispersed suspensions with partial absorbtion. The Rand Corporation, Santa Monica, California, Memorandum RM-3228-PR, 34 pp.
- Fujita, T., 1963b: Outline of a theory and examples for precise analysis of satellite radiation data. Mesomet. Project Res. Paper, No. 15, Univ. of Chicago, 35 pp.
- \_\_\_\_\_, 1964: The scanning printer and its application to detailed analysis of satellite radiation data. SMRP Res. Paper No. 34, Univ. of Chicago.
- \_\_\_\_\_, and H. Grandoso, 1966: A proposed method of estimating cloud-top temperature, cloud covers, and emissivity and whiteness of clouds from short- and long-wave radiation data obtained by TIROS scanning radiometers. SMRP Research Paper No. 48, Univ. of Chicago.
- Larsen, S. H. H., T. Fujita, W. L. Fletcher, 1963: TIROS III measurements of terrestrial radiation and reflected and scattered solar radiation. Mesomet. Project Res. Paper No. 20, Univ. of Chicago, 11 pp.
- Waldram, J. M., 1945: Measurement of the photometric properties of the upper atmosphere. Quart., J. R. meteor. Soc., 71, 319-336.
- Wiezee, W., and P. A. Davis, 1965: Evidence of the dependence of reflected solar radiation on viewing geometry in a TIROS IV radiation data sample. Journal of Appl. Meteorology, Volume 4, No. 5, 637-639.

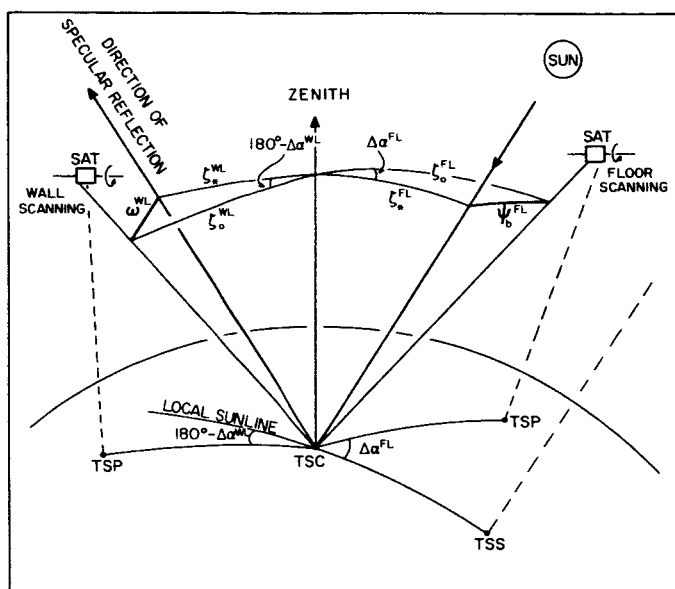


Fig. 1. Schematic view of the satellite scanning the same spot on the earth from two different positions. The specular angle,  $\omega^{WL}$ , and the backscattering angle,  $\psi_b^{FL}$ , are indicated by heavy lines.

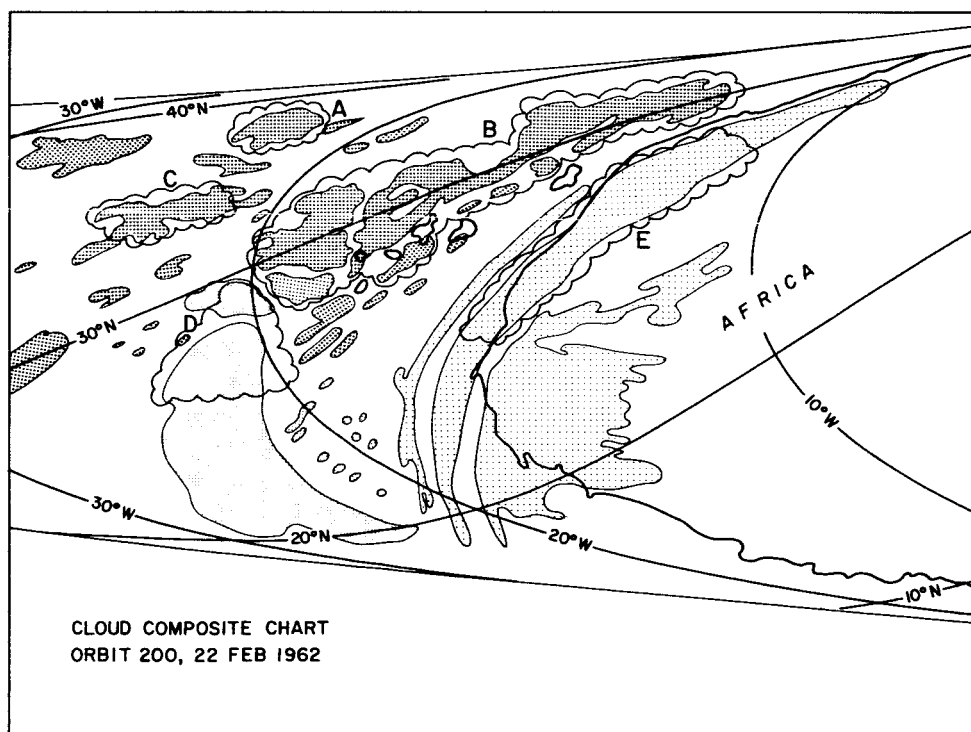


Fig. 2. Composite cloud chart from Orbit 200, TIROS IV, 22 February 1962. The clouds in the areas indicated by A, B, and C consist of low stratiform clouds, whereas the clouds in the areas D and E consist of altocumulus and cirrostratus, respectively.

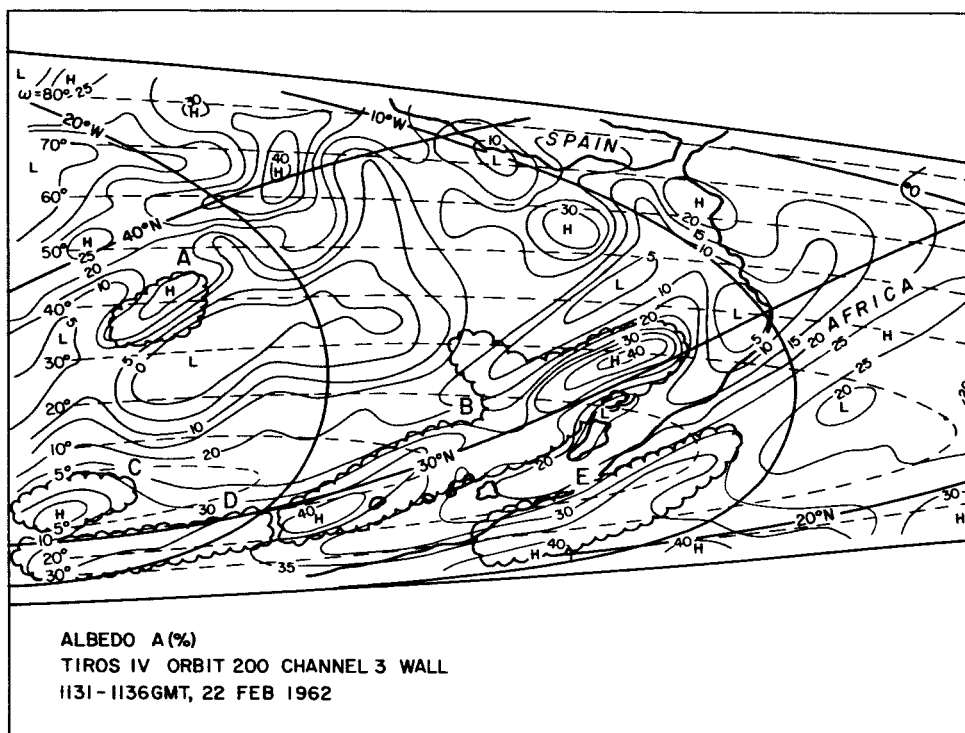


Fig. 3. Patterns of Channel 3 ( $0.25-6.0 \mu$ ) albedo A (%) received by the wall sensors during Orbit 200, TIROS IV, 22 February 1962. Isolines for the specular angle  $\omega^m$  are indicated by dashed lines. Longitude and latitude lines are drawn for every  $10^\circ$  interval, and coastlines are indicated by heavy lines.

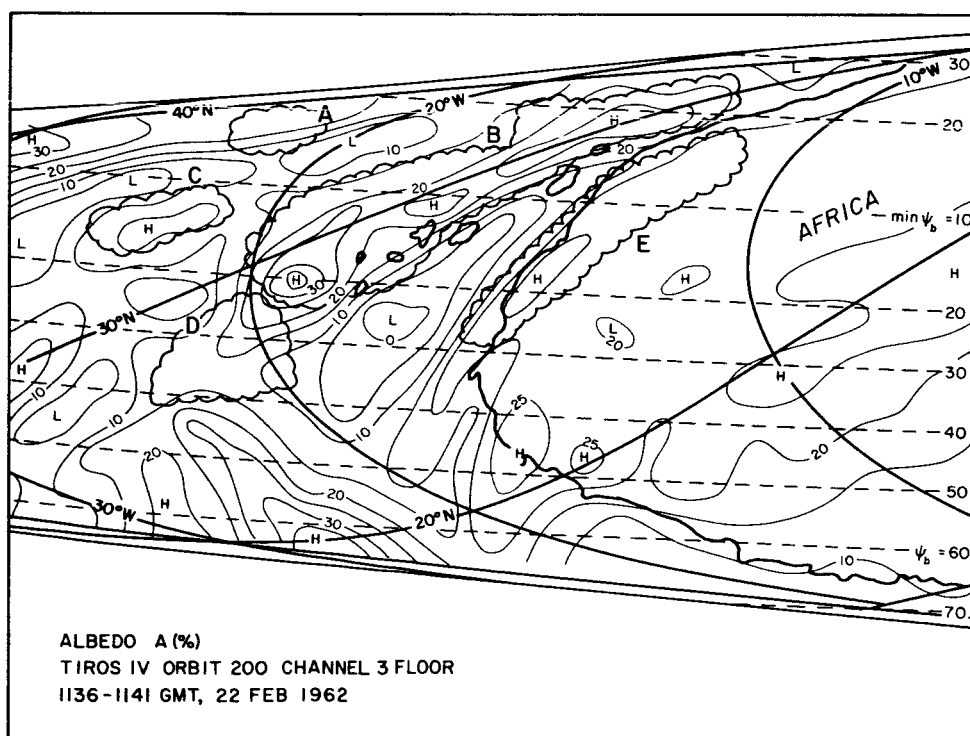


Fig. 4. Patterns of Channel 3, albedo A (%) received by the floor sensor during Orbit 200, TIROS IV, 22 February 1962. Isolines for the backscattering angle,  $\psi_b^{FL}$ , are indicated by dashed lines.

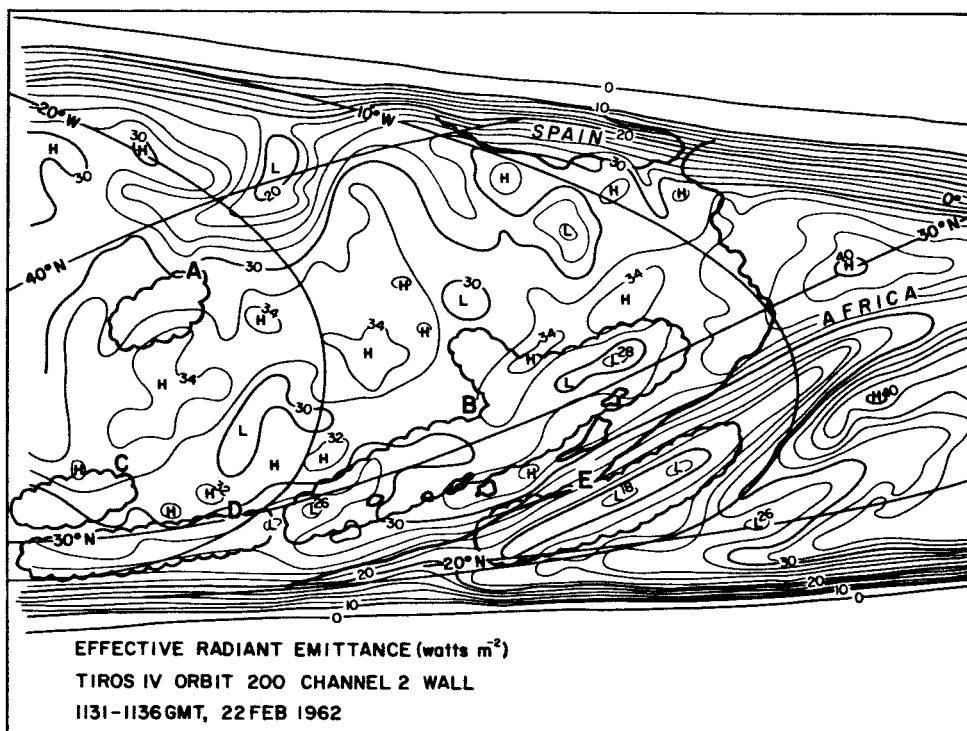


Fig. 5. Patterns of Channel 2 ( $8-12\mu$ ) effective radiant emittance  $\bar{W}$  (watts  $m^{-2}$ ) received by the wall sensor during Orbit 200, TIROS IV, 22 February 1962. Longitude and latitude lines are drawn for every  $10^\circ$  interval and the coastlines are indicated by heavy lines.

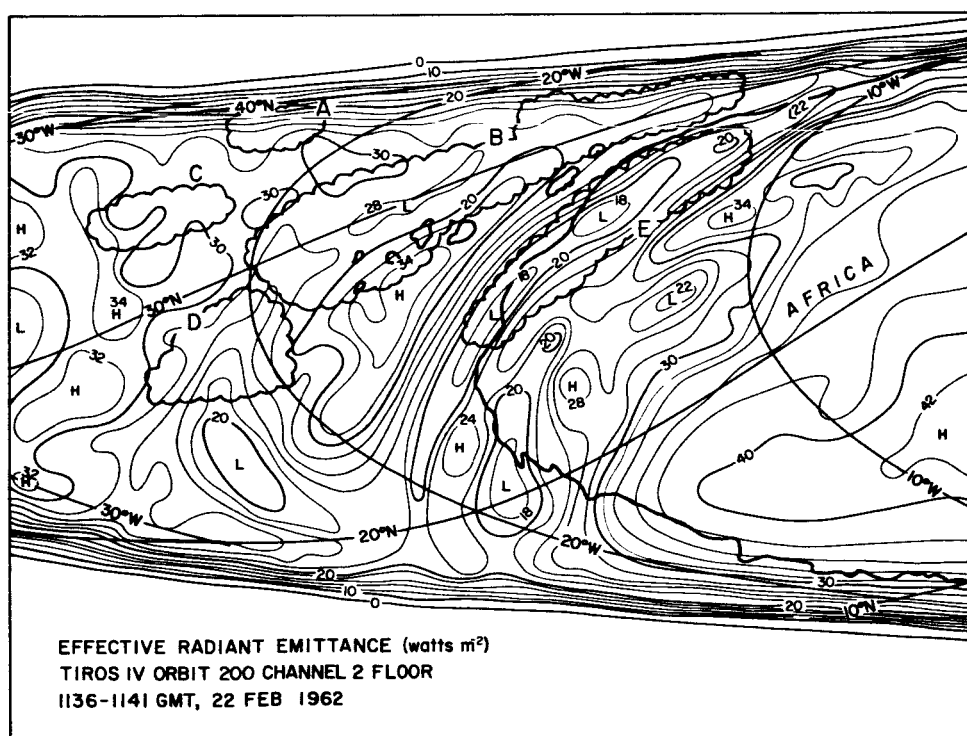


Fig. 6. Patterns of Channel 2 effective radiant emittance  $\bar{W}$  (watts  $m^{-2}$ ) received by the floor sensor during Orbit 200, floor sensor, TIROS IV, 22 February 1962.

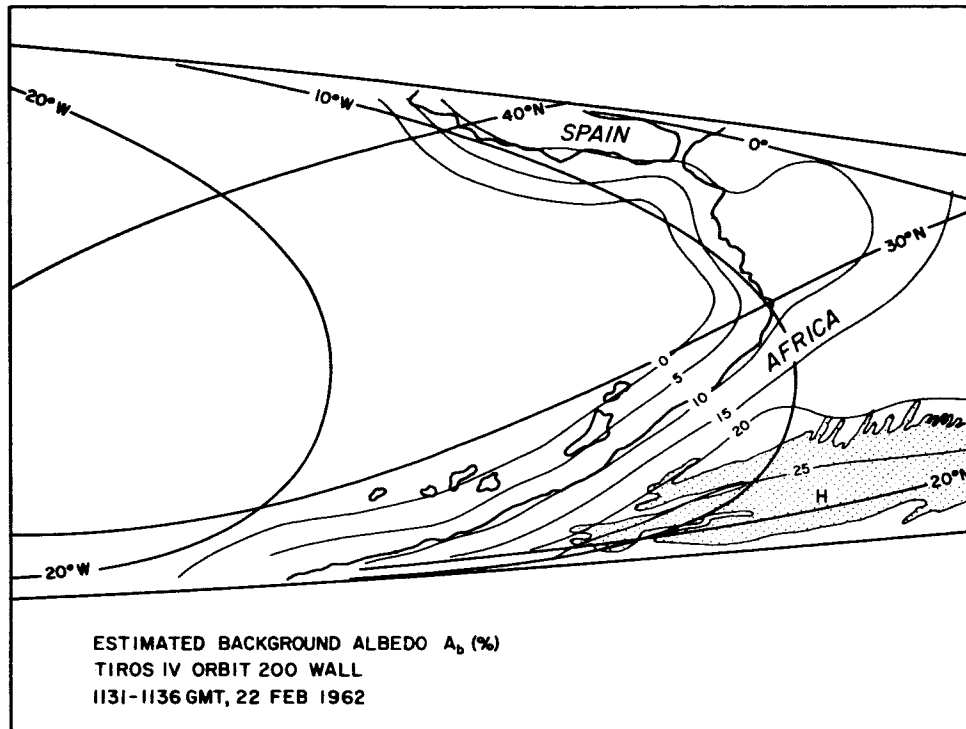


Fig. 7. Patterns of estimated background albedo  $A_b$  (%) for the wall sensor, Orbit 200, TIROS IV, 22 February 1962. The stippled area represents the Sahara Desert.

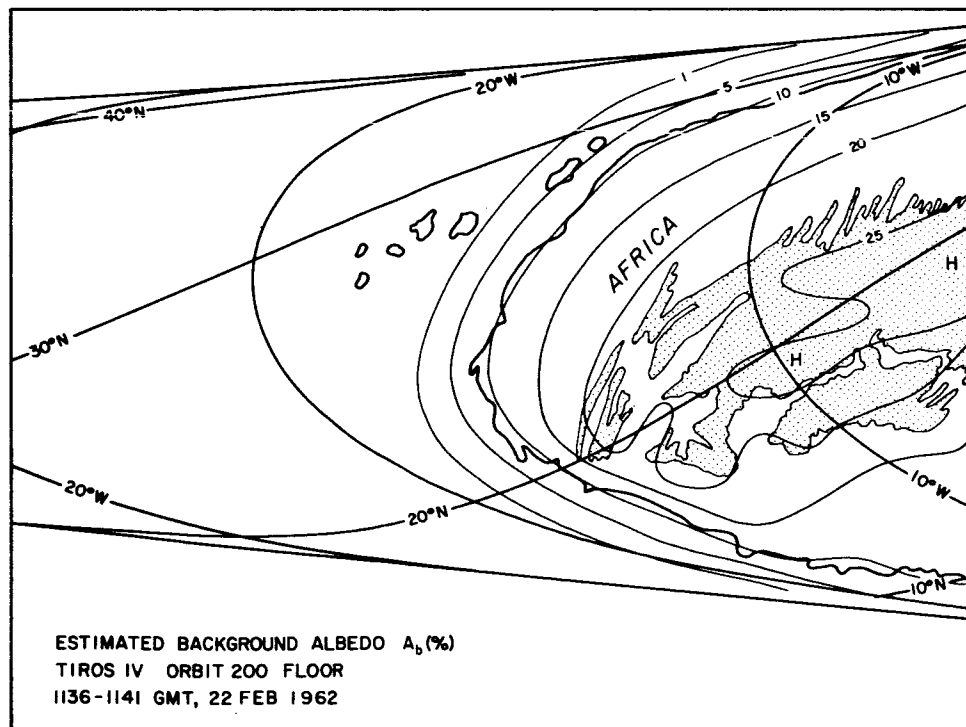


Fig. 8. Patterns of estimated background albedo  $A_b$  (%) for the floor sensor, Orbit 200, TIROS IV, 22 February 1962.



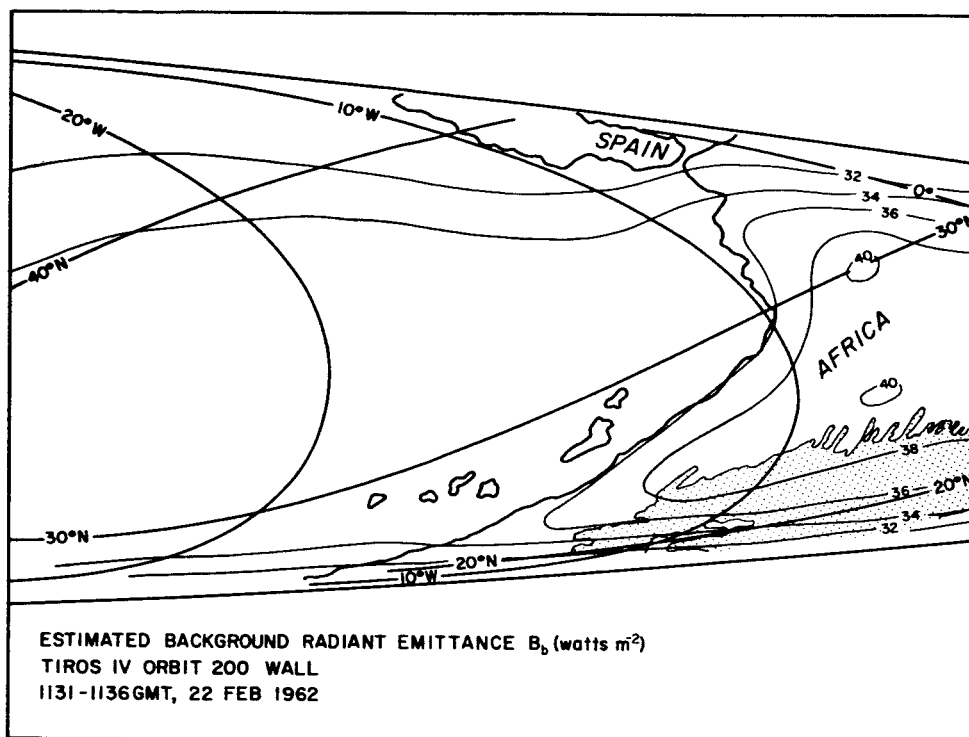


Fig. 9. Patterns of estimated effective background radiant emittance  $\bar{B}_b$  (watts  $m^{-2}$ ) for the wall sensor, Orbit 200, 22 February 1962. The stippled area represents the Sahara Desert.

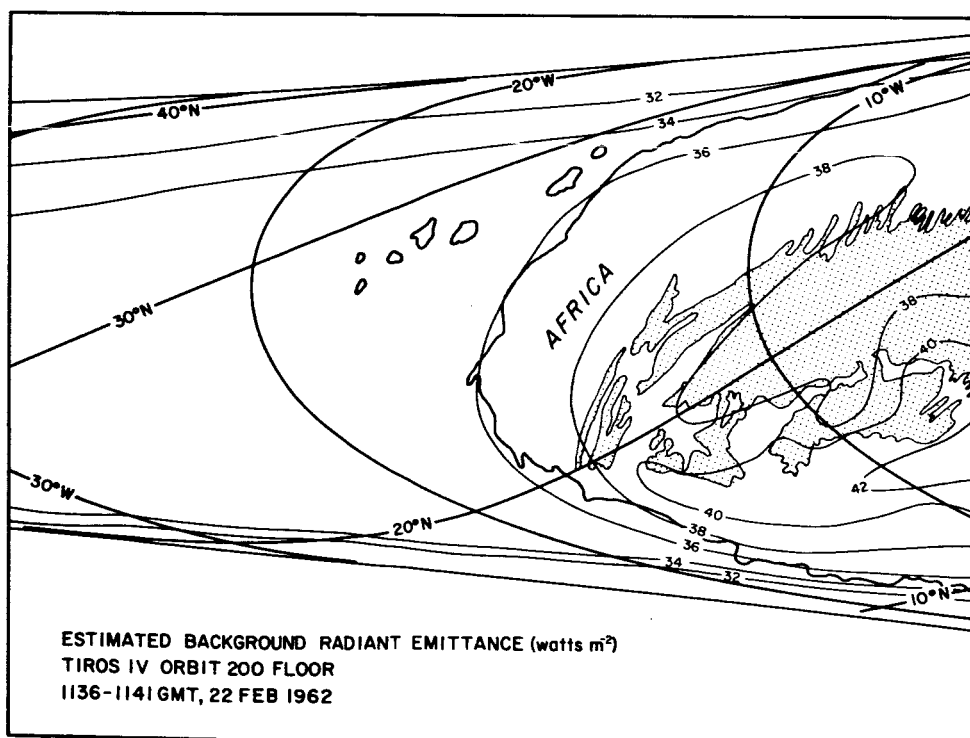


Fig. 10. Patterns of estimated effective background radiant emittance  $\bar{B}_b$  (watts  $m^{-2}$ ) for the floor sensor, Orbit 200, TIROS IV, 22 February 1962.

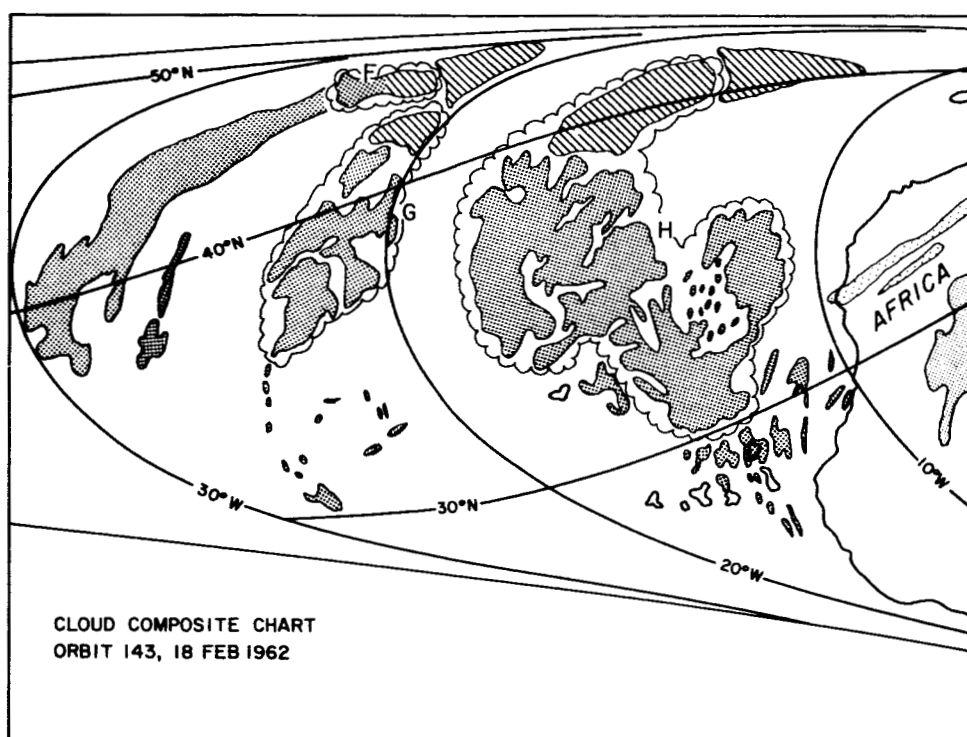


Fig. 11. Composite cloud chart from Orbit 143, TIROS IV, 18 February 1962. The clouds in the areas indicated by F, G, and H consist mainly in low stratiform clouds.

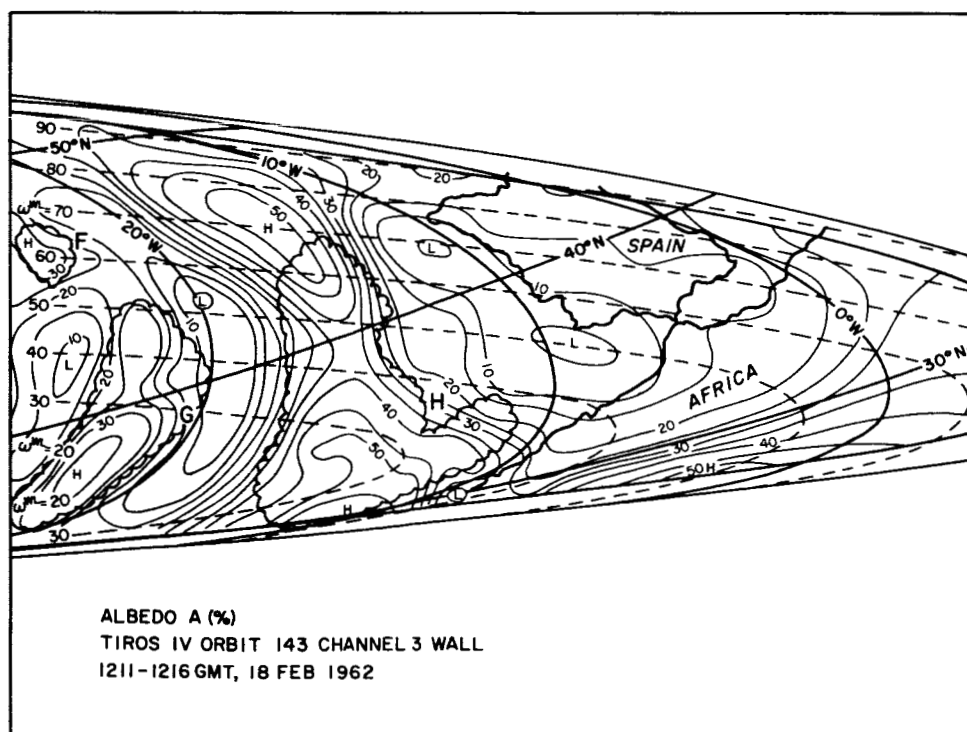


Fig. 12. Patterns of Channel 3 albedo A (%) received by the wall sensor during Orbit 143, TIROS IV, 18 February 1962. Isolines for the specular angle  $\omega^m$  are indicated by dashed lines.

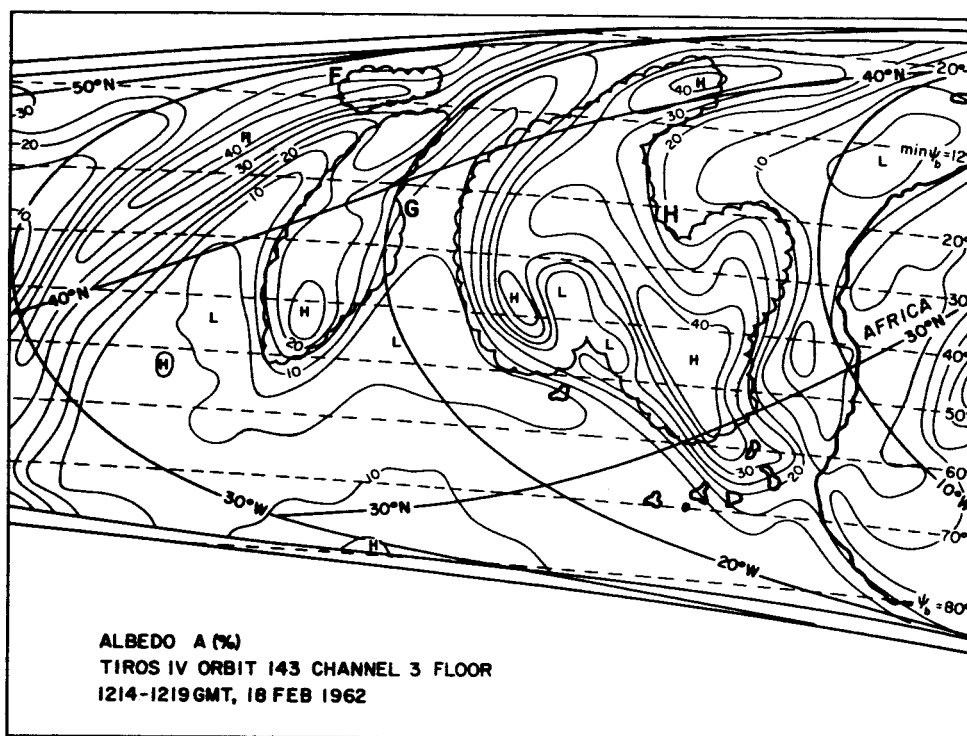


Fig. 13. Patterns of Channel 3 albedo  $A$  (%) received by the floor sensor during Orbit 143, TIROS IV, 18 February 1962. Isolines for the backscattering angles  $\psi_b^{FL}$  are indicated by dashed lines.

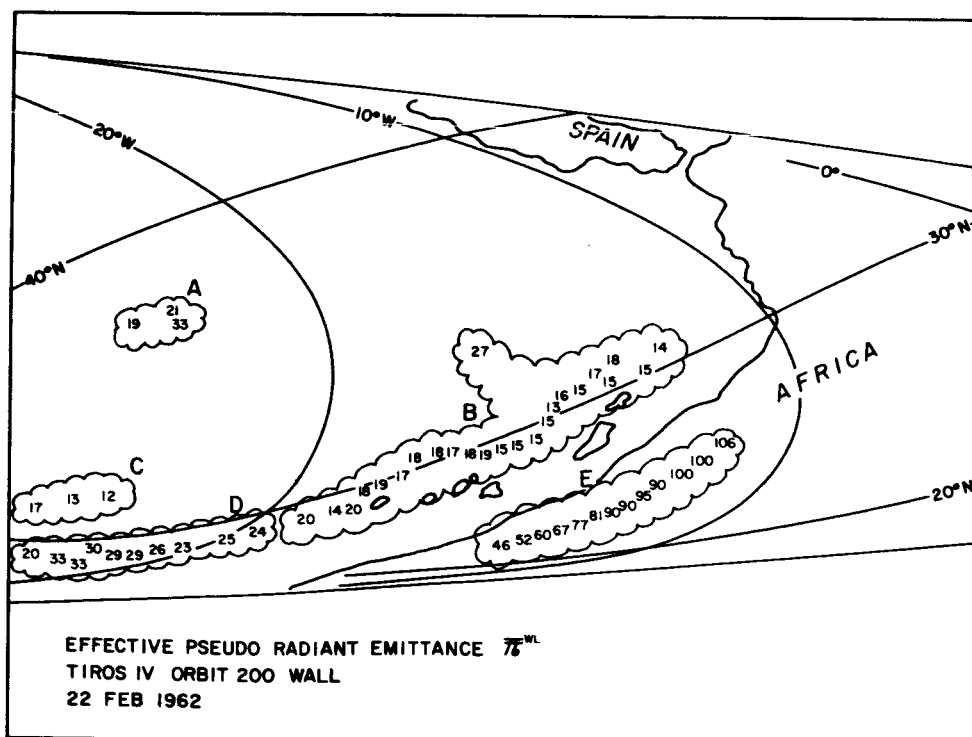


Fig. 14. Computed effective pseudo-radiant emittance  $\pi^{WL}$  of the cloudy areas indicated by A, B, C, D, and E for the wall sensor, Orbit 200, TIROS IV, 22 February 1962.

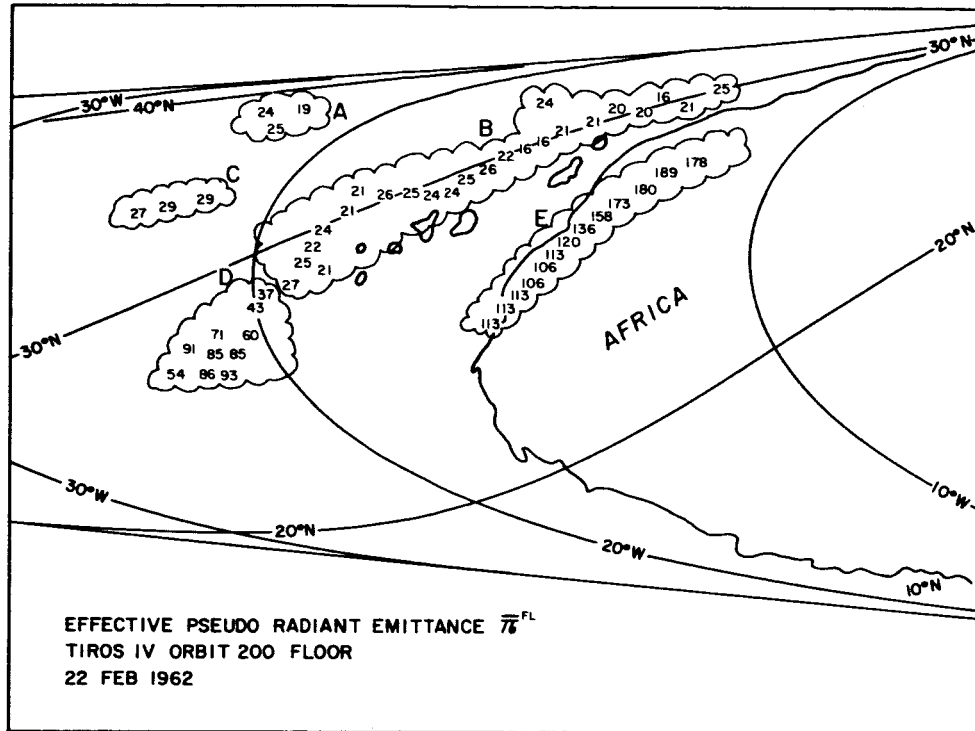


Fig. 15. Computed effective pseudo-radiant emittance  $\bar{\pi}^{FL}$  of the cloudy areas indicated by A, B, C, D, and E for the floor sensor, Orbit 200, TIROS IV, 22 February 1962.

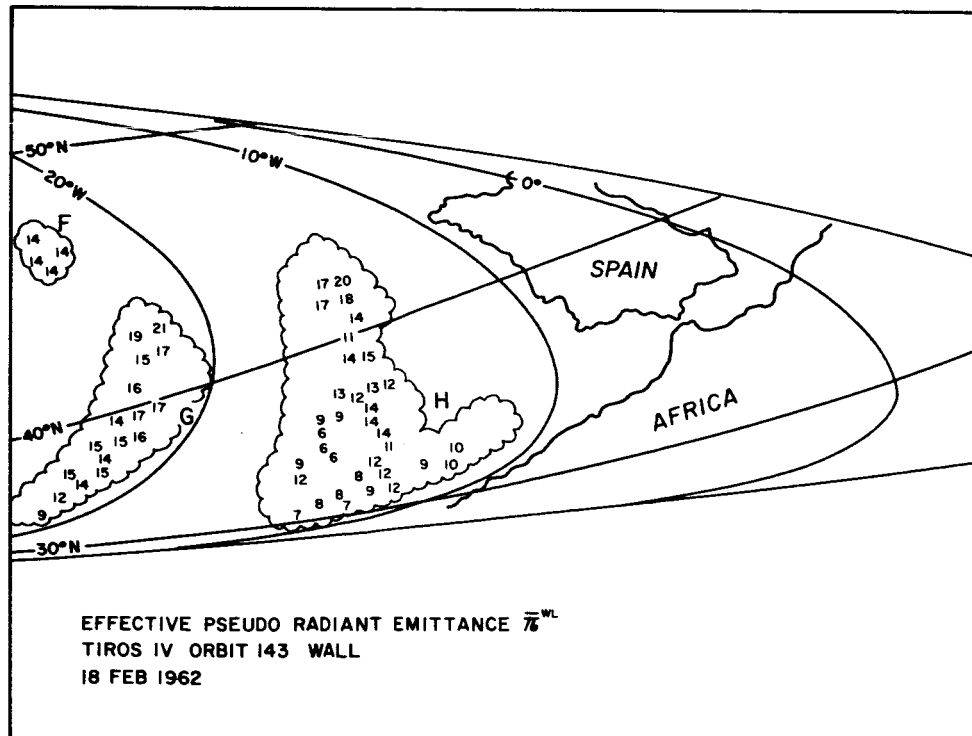


Fig. 16. Computed effective pseudo-radiant emittance  $\bar{\pi}^{WL}$  of the cloudy areas indicated by F, G, and H for the wall sensor, Orbit 143, TIROS IV, 18 February 1962.

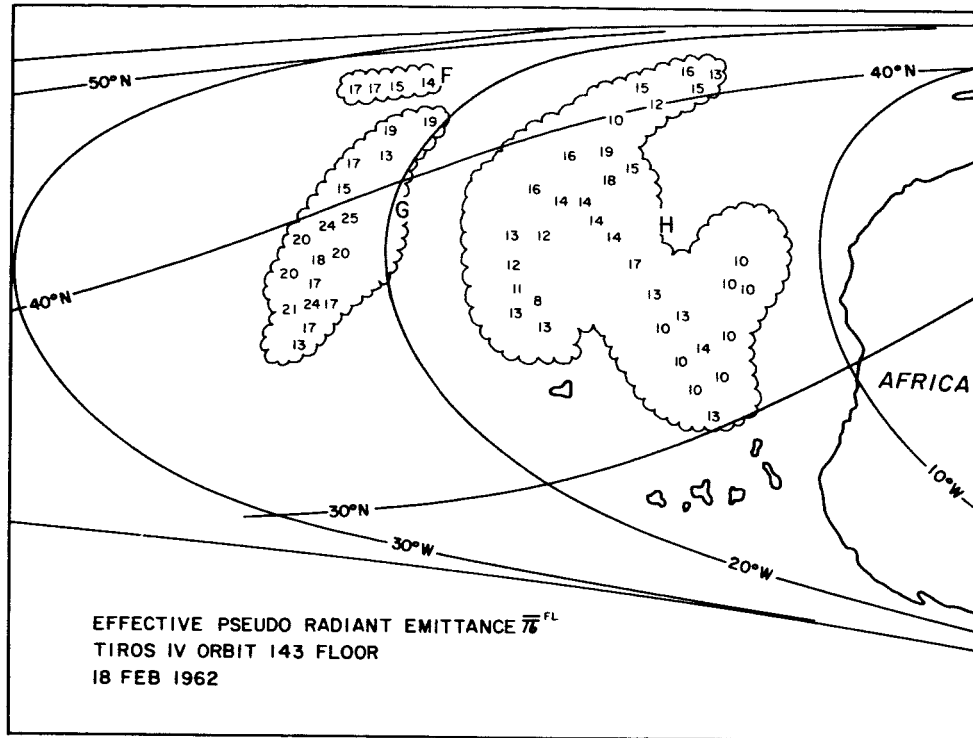


Fig. 17. Computed effective pseudo-radiant emittance  $\overline{\pi}^{FL}$  of the cloudy areas indicated by F, G, and H for the floor sensor, Orbit 143, TIROS IV, 18 February 1962.

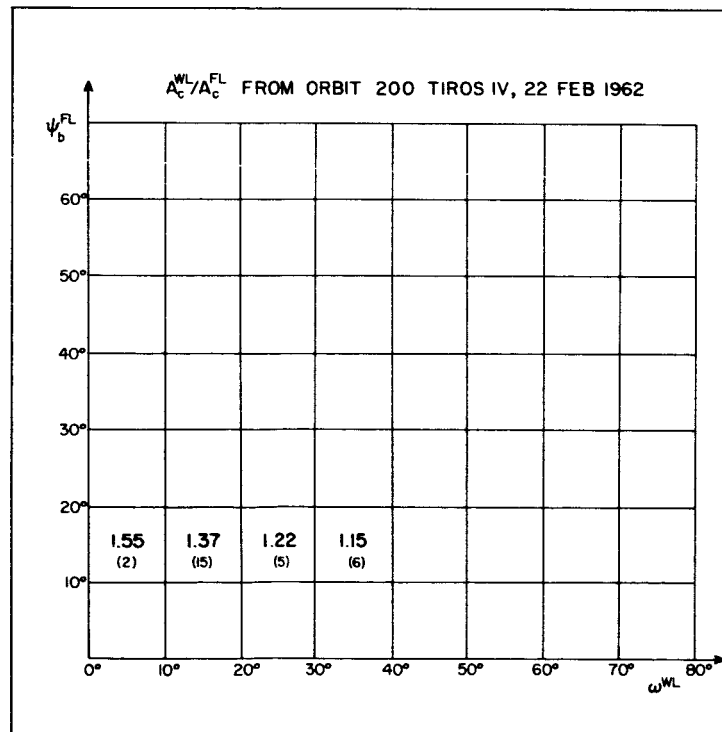


Fig. 18. The ratio,  $A_c^{WL}/A_c^{FL}$ , between the cloud albedo to the wall sensor and the cloud albedo to the floor sensor as a function of the specular angle of the wall sensor,  $\omega^{WL}$ , and the backscattering angle of the floor sensor,  $\psi_b^{FL}$ . TIROS IV, Orbit 200, 22 February 1962.

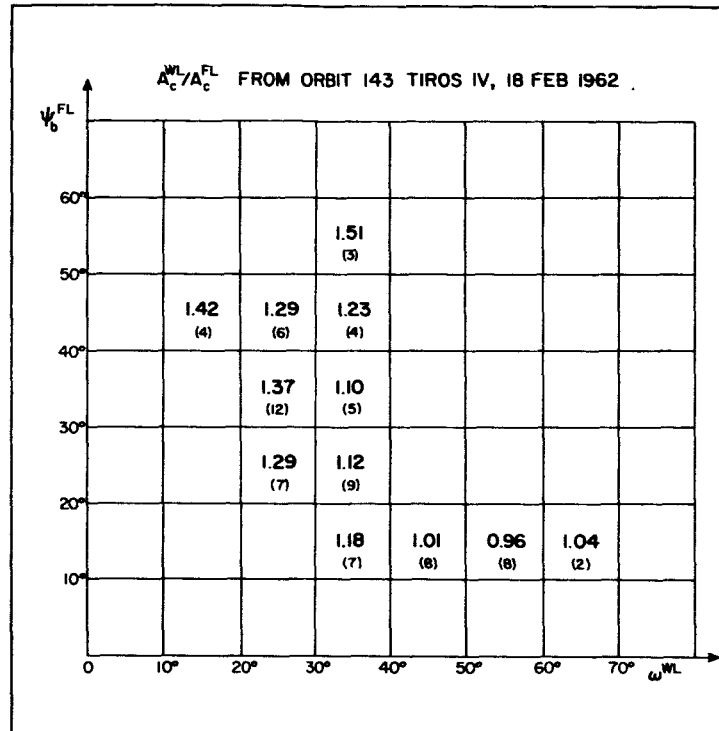


Fig. 19. The ratio,  $A_c^{WL}/A_c^{FL}$ , plotted as a function of the specular angle  $\omega^{WL}$  and the backscattering angle  $\psi_0^{FL}$ . TIROS IV, Orbit 143, 18 February 1962.

MESOMETEOROLOGY PROJECT - - - RESEARCH PAPERS

(Continued from front cover)

42. A Study of Factors Contributing to Dissipation of Energy in a Developing Cumulonimbus - Rodger A. Brown and Tetsuya Fujita
43. A Program for Computer Gridding of Satellite Photographs for Mesoscale Research - William D. Bonner
44. Comparison of Grassland Surface Temperatures Measured by TIROS VII and Airborne Radiometers under Clear Sky and Cirriform Cloud Conditions - Ronald M. Reap
45. Death Valley Temperature Analysis Utilizing Nimbus I Infrared Data and Ground-Based Measurements - Ronald M. Reap and Tetsuya Fujita
- t 46. On the "Thunderstorm-High Controversy" - Rodger A. Brown
47. Application of Precise Fujita Method on Nimbus I Photo Gridding - Lt. Cmd. Ruben Nasta
48. A Proposed Method of Estimating Cloud-top Temperature, Cloud Cover, and Emissivity and Whiteness of Clouds from Short- and Long-wave Radiation Data Obtained by TIROS Scanning Radiometers - T. Fujita and H. Grandoso
49. Aerial Survey of the Palm Sunday Tornadoes of April 11, 1965 - Tetsuya Fujita
50. Early Stage of Tornado Development as Revealed by Satellite Photographs - Tetsuya Fujita
51. Features and Motions of Radar Echoes on Palm Sunday, 1965 - D. L. Bradbury and Tetsuya Fujita
52. Stability and Differential Advection Associated with Tornado Development - Tetsuya Fujita and Dorothy L. Bradbury
53. Estimated Wind Speeds of the Palm Sunday Tornadoes - Tetsuya Fujita
54. On the Determination of Exchange Coefficients: Part II - Rotating and Nonrotating Convective Currents - Rodger A. Brown
55. Satellite Meteorological Study of Evaporation and Cloud Formation over the Western Pacific under the Influence of the Winter Monsoon - K. Tsuchiya and T. Fujita
56. A Proposed Mechanism of Snowstorm Mesojet over Japan under the Influence of the Winter Monsoon - T. Fujita and K. Tsuchiya
57. Some Effects of Lake Michigan upon Squall Lines and Summertime Convection - Walter A. Lyons